

# <sup>1</sup> Spatio-Temporal Graph Neural Networks for Regional Groundwater <sup>2</sup> Level Forecasting: A Case Study of the Haouz Aquifer, Morocco

<sup>3</sup> Author 1<sup>a</sup>, Author 2<sup>b</sup> and Author 3<sup>c</sup>

4

---

## <sup>5</sup> ARTICLE INFO

6

**Keywords:**

Graph convolutional network

Long short-term memory

Groundwater forecasting

Spatiotemporal graph neural networks

13

14

15

16

17

18

19

---

## ABSTRACT

Groundwater plays a critical role in sustaining ecosystems, agriculture, and human water demand. Accurate forecasting of groundwater levels is essential for sustainable water resource management, particularly in regions experiencing climate change and increasing demand. Traditional time-series and statistical models often struggle to capture the nonlinear dependencies and spatial interactions inherent in groundwater systems. This paper explores the application of Spatio-Temporal Graph Neural Networks (STGNNs) for groundwater level forecasting. By modeling monitoring wells as nodes and hydrological, geological, and climatic relationships as graph edges, STGNNs effectively capture both spatial dependencies and temporal dynamics. The findings highlight the potential of graph-based deep learning methods as a valuable tool for groundwater monitoring and management.

## <sup>20</sup> CRediT authorship contribution statement

<sup>21</sup> **Author 1:** contribution . **Author 2:** contribution . **Author 3:** contribution.

## <sup>22</sup> 1. Introduction

<sup>23</sup> Groundwater is an indispensable natural resource that sustains ecosystems, supports intensive agriculture, and  
<sup>24</sup> fulfills domestic and industrial demands worldwide. As one of the primary freshwater reservoirs, it plays a critical role  
<sup>25</sup> in mitigating the impacts of droughts and maintaining water security, particularly in semi-arid and arid regions where  
<sup>26</sup> surface water availability is increasingly erratic [Scanlon et al. \(2023\)](#). However, mounting anthropogenic pressures and  
<sup>27</sup> the accelerating effects of climate change manifested through irregular precipitation patterns, rising temperatures, and  
<sup>28</sup> land-use transformations pose unprecedented challenges to groundwater sustainability [Taylor et al. \(2013\)](#); [Famiglietti](#)  
<sup>29</sup> ([2014](#)). Over-extraction for irrigation and inadequate recharge have contributed to alarming declines in groundwater  
<sup>30</sup> levels (GWLS) across many major aquifers, leading to long-term ecological degradation and severe socio-economic  
<sup>31</sup> consequences [Wada et al. \(2010\)](#); [Mukherjee et al. \(2024\)](#).

### <sup>32</sup> 1.1. Challenges in Groundwater Modeling

<sup>33</sup> In this context of scarcity and stress, accurate and timely forecasting of GWLS is a prerequisite for sustainable water  
<sup>34</sup> resource management, efficient irrigation planning, and drought mitigation [Sun et al. \(2022\)](#). Yet, modeling ground-  
<sup>35</sup> water dynamics remains a formidable challenge due to the nonlinear interactions between meteorological drivers, hy-  
<sup>36</sup> drological processes, geological heterogeneity, and anthropogenic interventions such as pumping [Sophocleous \(2002\)](#).

---

ORCID(s): 0009-0007-8193-5359 (A. 1)

37 Historically, hydrogeologists have relied on physically-based models (e.g., MODFLOW). While these models are  
 38 grounded in physical laws and provide robust understanding of flow dynamics [Anderson et al. \(2015\)](#), they require  
 39 extensive site-specific hydrogeological data—often unavailable in data-scarce regions—and involve computationally  
 40 intensive parameterization and calibration processes [Refsgaard \(1997\)](#). Alternatively, geostatistical approaches, while  
 41 valuable for spatial interpolation, typically assume stationarity and linear relationships, limiting their capacity to ex-  
 42 trapolate under the non-stationary conditions induced by climate change.

### 43 **1.2. The Evolution from Temporal ML to Spatio-Temporal Deep Learning**

44 To overcome the limitations of physical and statistical models, data-driven Machine Learning (ML) and Deep  
 45 Learning (DL) approaches have gained prominence in recent decades. Early applications utilizing Artificial Neural  
 46 Networks (ANNs), Support Vector Machines (SVMs), and Random Forests (RF) demonstrated superior performance  
 47 in capturing nonlinear relationships compared to traditional multiple linear regression [Nayak et al. \(2006\)](#); [Sahoo and](#)  
 48 [Jha \(2013\)](#). More recently, Recurrent Neural Networks (RNNs), and specifically Long Short-Term Memory (LSTM)  
 49 networks, have become the state of the art for hydrological time series forecasting due to their ability to learn long  
 50 term temporal dependencies [Lin et al. \(2022\)](#).

51 However, a critical methodological gap persists: standard deep learning models like LSTM typically treat monitor-  
 52 ing wells as isolated entities. They rely exclusively on temporal sequences, ignoring the *spatial dependencies* inherent  
 53 in an aquifer system [Li et al. \(2023\)](#). Groundwater levels in a monitoring network are not independent; they are physi-  
 54 cally interconnected through hydraulic gradients, where fluctuations in one well are influenced by pumping, recharge,  
 55 and geological conditions at neighboring locations [Chang et al. \(2025\)](#). Neglecting this spatial interconnectivity lim-  
 56 its the predictive accuracy and physical interpretability of forecasting models, particularly in complex, over-exploited  
 57 aquifers.

### 58 **1.3. The Emergence of Spatio-Temporal Graph Neural Networks (STGNNs)**

59 To address the dual challenge of spatial complexity and temporal dynamism, Graph Neural Networks (GNNs)  
 60 have emerged as a transformative framework. By representing monitoring wells as nodes and their hydrogeological  
 61 relationships as edges in a graph structure, GNNs explicitly encode spatial dependencies [Scarselli et al. \(2009\)](#); [Kipf](#)  
 62 [and Welling \(2017\)](#). Recent advancements have extended this paradigm to Spatio-Temporal Graph Neural Networks  
 63 (STGNNs), which integrate graph convolutions (to capture spatial features) with sequence learning modules (to capture  
 64 temporal dynamics) [Yu et al. \(2018\)](#); [Sahili and Awad \(2023\)](#).

65 The application of STGNNs to groundwater forecasting represents the cutting edge of hydro-informatics. Recent  
 66 studies have demonstrated that these architectures significantly outperform traditional ML and temporal-only DL mod-  
 67 els. For instance, Bai and Tahmasebi [Bai and Tahmasebi \(2023\)](#) utilized a GNN with a self-adaptive adjacency matrix

68 to forecast GWLs, proving the model could learn spatial dependencies even when physical connectivity data was in-  
 69 complete. Similarly, Taccari et al. [Taccari et al. \(2024\)](#) applied STGNNs to the Overbetuwe area in the Netherlands,  
 70 effectively integrating auxiliary variables like precipitation and evaporation to handle missing data robustly. Further-  
 71 more, Liang et al. [Liang et al. \(2025\)](#) proposed a GCN-LSTM framework to serve as a computationally efficient  
 72 surrogate for numerical models in Quebec, highlighting the scalability of the approach. Recent work by Wu et al. [Wu](#)  
 73 [et al. \(2025\)](#) further characterized multiple spatial dependencies such as hydraulic gradients and sub-basin delineations  
 74 demonstrating that capturing these complex interactions is vital for regional forecasting.

#### 75 **1.4. Contextualizing the Study: The Haouz Region, Morocco**

76 Despite these global advancements, the application of STGNNs in the specific context of North African semi-arid  
 77 aquifers remains unexplored. The Haouz region in Morocco exemplifies the "data-scarce" and "high-stress" environ-  
 78 ments where such advanced modeling is most needed [Borzi \(2025\)](#). Similar to the situation in the Rabat-Salé-Kénitra  
 79 region [Elmotawakkil and Enneya \(2024\)](#), the Haouz aquifer faces severe depletion due to intensive irrigation and re-  
 80 current drought. While recent local studies have employed dimensionality reduction and neural networks to analyze  
 81 these trends [Bouramtane et al. \(2025\)](#), they have largely relied on temporal correlations, leaving the spatial network  
 82 dynamics unmodeled.

83 The complex subsurface geometries and hydrogeological challenges observed in regions such as the Al Haouz Mej-  
 84 jate basin characterized by intensive groundwater abstraction and limited natural recharge require advanced modeling  
 85 approaches to reliably estimate aquifer substrate topography and predict groundwater dynamics [El Mezouary et al.](#)  
 86 [\(2024\)](#). Recent studies have demonstrated that nonlinear machine learning techniques, including Gaussian Process  
 87 Regression and deep neural network architectures, can effectively infer substrate depths by integrating sparse bore-  
 88 hole information with regional geospatial datasets, achieving coefficient of determination ( $R^2$ ) values exceeding 0.8  
 89 when validated against independent borehole measurements [El Mezouary et al. \(2024\)](#). These findings highlight the  
 90 growing potential of data-driven computational frameworks for characterizing key hydraulic parameters of ground-  
 91 water reservoirs, parameters that are traditionally costly, time-consuming, and often uncertain when estimated solely  
 92 through field-based investigations.

#### 93 **1.5. Research Objectives and Contribution**

94 This study aims to bridge this research gap by introducing a Spatio-Temporal Graph Convolutional Network  
 95 (STGCN) framework specifically tailored for the Haouz aquifer. By conceptualizing the monitoring network as a  
 96 dynamic graph, we move beyond isolated time-series analysis to explicitly model the hydraulic connectivity between  
 97 wells.

98 The main contributions of this study are as follows:

- 99     1. **Methodological Innovation:** We develop a unified STGNN forecasting framework that integrates hydrological  
 100 and climatic dependencies, addressing the limitations of standard LSTM models in capturing spatial correlations  
 101 Wang et al. (2024); Chen et al. (2025).
- 102     2. **Regional Application:** We provide the first application of STGCN for GWL forecasting in the Haouz region,  
 103 offering a high-accuracy tool for managing groundwater resources under conditions of data scarcity and climate  
 104 stress Talib et al. (2024).
- 105     3. **Benchmarking and Validation:** We comprehensively benchmark the proposed approach against traditional  
 106 deep learning (LSTM, GRU) baselines, demonstrating superior predictive performance and stability.
- 107     4. **Decision Support:** We highlight the potential of the graph-based approach to serve as a decision-support tool,  
 108 facilitating interpretable and scalable management strategies for the Haouz basin Mahammad et al. (2023).

## 109     2. Methodology

### 110     2.1. Data Collection

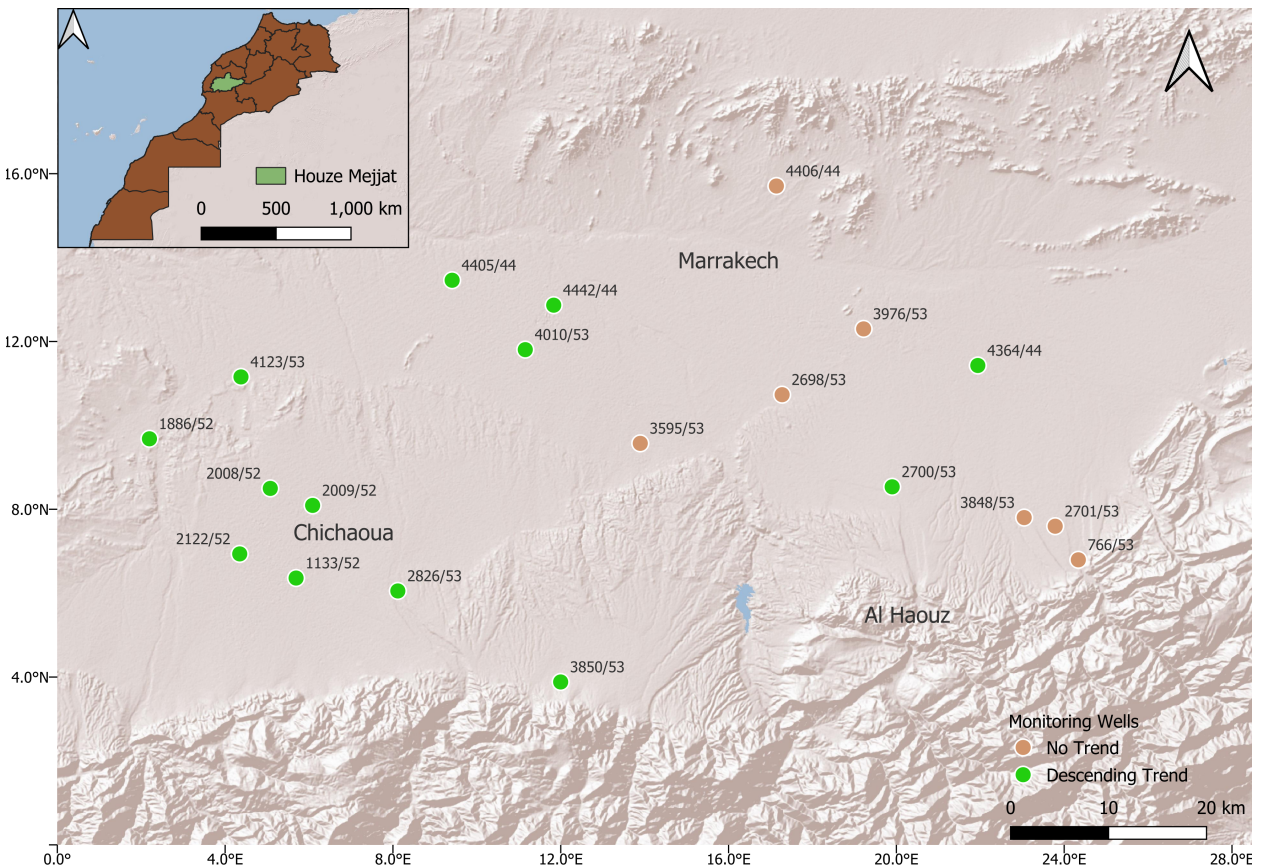


**Figure 1:** Location of the study area and monitoring wells, the brown dots indicates wells where the ground water level has an obvious trend, the green dots indicates wells with no trend.

111 Groundwater level data are typically obtained from monitoring well networks from the Tensift Hydraulic Basin  
 112 Agency (Agence des Bassins Hydraulique du Tensift, ABHT <https://abht.ma/>). Supplementary variables such as pre-  
 113 cipitation, evapotranspiration, soil moisture, and land surface temperature can improve forecasting accuracy 'CITE'.

114 The primary dataset used in this study consists of groundwater level (GWL) observations collected from a network  
 115 of monitoring wells located within the study area. These measurements are available at a monthly temporal resolution  
 116 and represent the target variable for the forecasting task. Each well provides a continuous time series of groundwater  
 117 levels, allowing for the characterization of seasonal and interannual variations in groundwater storage.

118 To improve the predictive capacity of the forecasting models, complementary hydro-meteorological and land-  
 119 surface variables were integrated. These explanatory variables were selected based on their relevance to groundwater  
 120 recharge and depletion processes, and were obtained from a combination of remote sensing products and reanalysis  
 121 datasets:

122 • **Precipitation:** Obtained from the CHIRPS dataset [Funk et al. \(2015\)](#), which provides quasi-global rainfall  
 123 estimates at high spatial resolution.

124 • **Evapotranspiration (ET):** Extracted from the FAO WaPOR database [Food and Agriculture Organization of the](#)  
 125 [United Nations \(FAO\) \(2020\)](#), offering spatially explicit data on actual evapotranspiration.

126 • **Land Surface Temperature (LST):** Retrieved from MODIS MOD11C3/MYD11C3 products [Wan et al. \(2021\)](#).

127 • **Normalized Difference Vegetation Index (NDVI):** Acquired from the MODIS MOD13Q1 vegetation index  
 128 dataset [Didan \(2021\)](#).

129 • **Soil Moisture and Soil Temperature:** Taken from the ERA5 reanalysis dataset [Rodell et al. \(2004\)](#).

130 All variables were collected at a monthly temporal scale and spatially aligned with the locations of the monitoring  
 131 wells. When necessary, gridded datasets were resampled to match the geographic coordinates of the wells, ensuring  
 132 consistency across time series inputs. The resulting multi-source dataset thus combines in situ observations with  
 133 satellite-derived indicators of hydrological processes.

134 To illustrate the temporal variability of the datasets, exploratory plots were generated. Figure 2 presents the monthly  
 135 evolution of groundwater levels alongside selected climatic and land-surface variables for representative wells. These  
 136 visualizations highlight the seasonal cycles and potential lagged relationships between groundwater response and cli-  
 137 matic drivers.

138 Figure 3 illustrates the temporal evolution of groundwater levels for a selection of monitoring wells within the  
 139 study area. Several important observations can be made from these plots. First, clear declining trends are visible in a  
 140 number of wells, suggesting sustained groundwater depletion likely associated with long-term pumping for irrigation

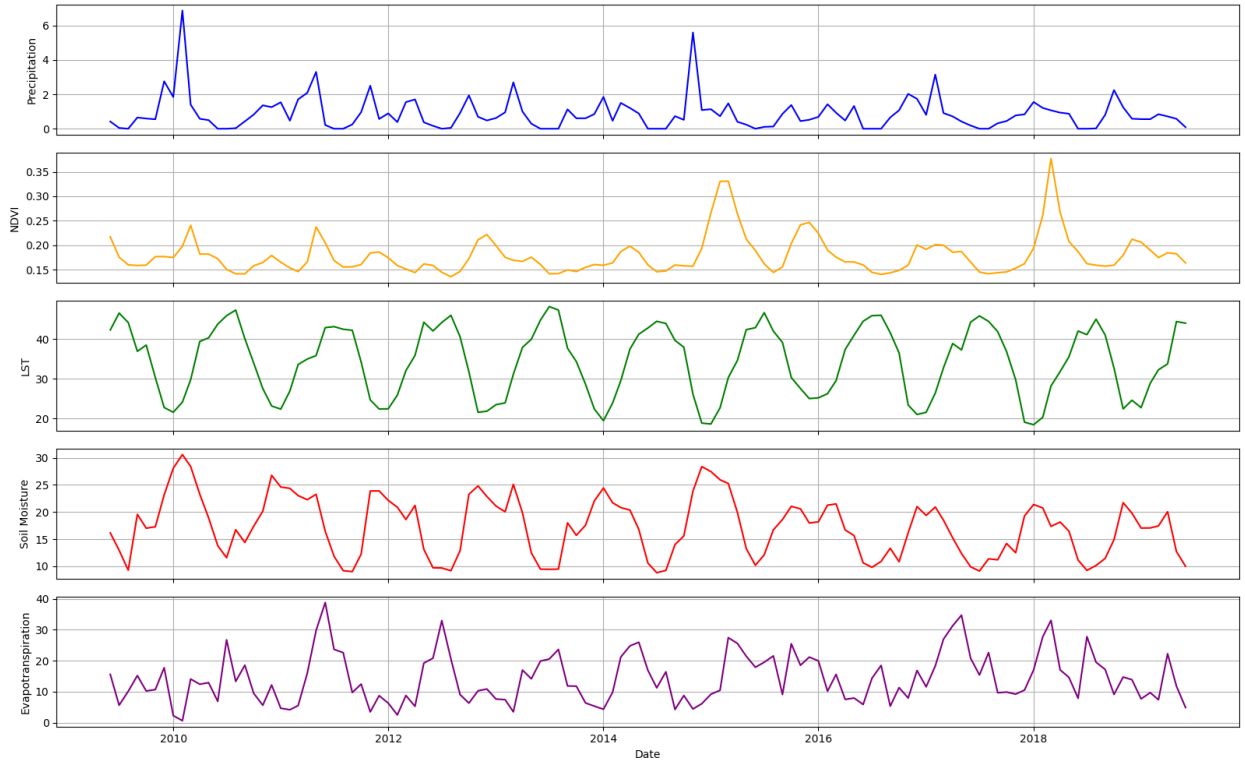


**Figure 2:** Example of temporal evolution of a selected explanatory variables for a representative well.

141 and domestic use. In contrast, other wells exhibit more stable or fluctuating dynamics, indicating that groundwater  
142 responses are not uniform across the aquifer system.

143 The variability observed between wells highlights the combined influence of multiple controlling factors. Anthro-  
144 pogenic drivers, such as groundwater abstraction rates and land-use practices, exert a strong influence in certain areas.  
145 At the same time, natural processes such as snow accumulation and melt, precipitation variability, soil moisture con-  
146 ditions, and evapotranspiration patterns also contribute to the temporal evolution of groundwater levels. The interplay  
147 of these factors introduces significant spatial heterogeneity, making groundwater forecasting a challenging task. These  
148 observations emphasize the need to integrate complementary hydro-meteorological variables alongside groundwater  
149 measurements when developing predictive models.

## 150 **2.2. Data Preprocessing**

151 The raw datasets required preprocessing to ensure consistency across the time series and to filter out irrelevant  
152 predictors.

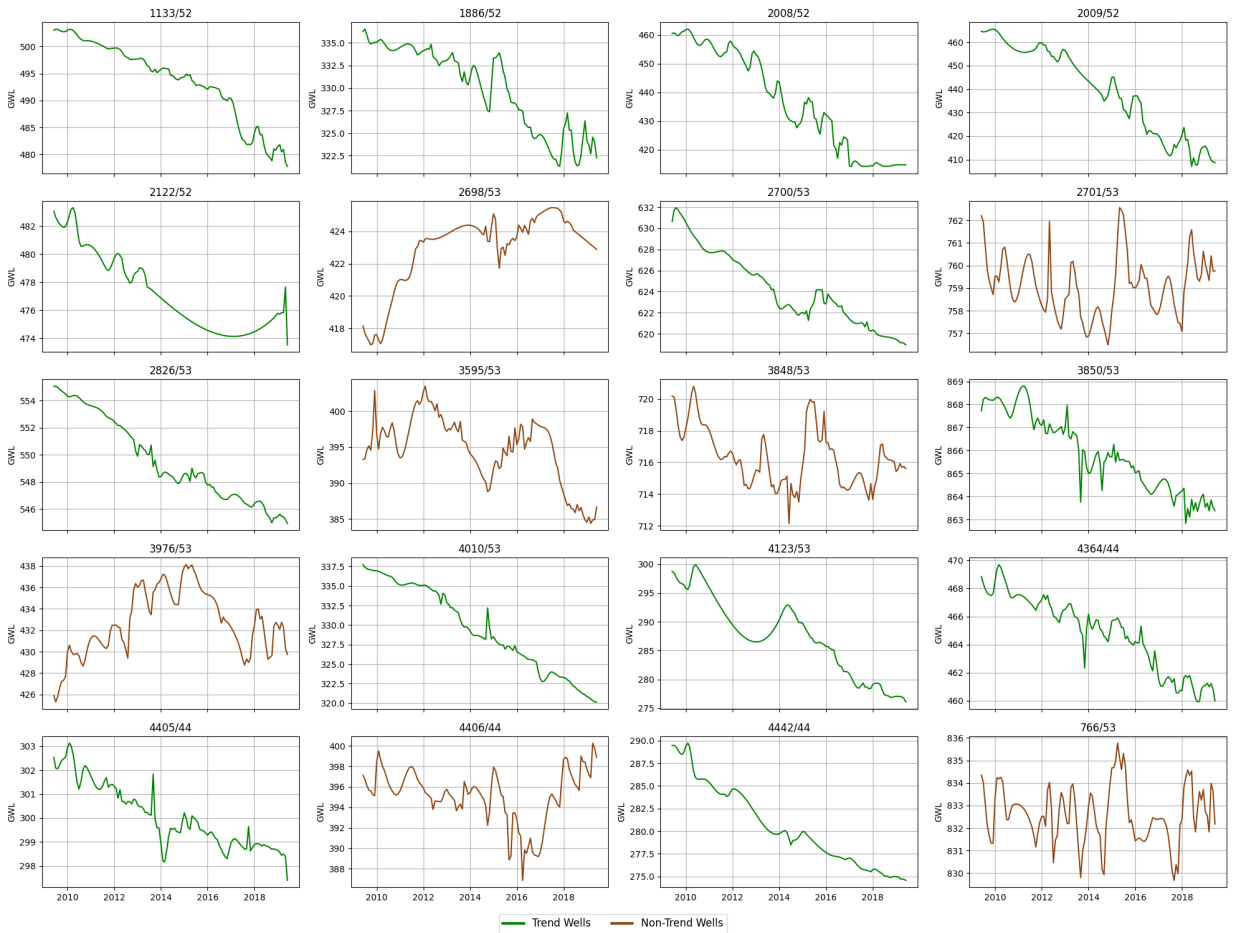


**Figure 3:** Temporal evolution of groundwater levels for all the wells used in the dataset. The plots highlight both declining trends in some wells and heterogeneous dynamics across the study area.

### 153 **Groundwater Level Standardization**

154 The raw groundwater level measurements were often collected at irregular intervals, ranging from daily to quarterly  
 155 observations depending on the well. To standardize the temporal resolution, the data were aggregated into monthly time  
 156 steps. For months containing multiple readings, the mean groundwater level was calculated; for months with single  
 157 readings, that value was retained. Following this aggregation, gaps remained in the time series, typically corresponding  
 158 to missing months. To reconstruct continuous sequences, these missing values were imputed using polynomial inter-  
 159 polation. This approach preserves the general temporal dynamics of the series while minimizing distortions introduced  
 160 by missing data.

### 161 **Feature Selection**

162 Initially, a broad set of potential explanatory variables was considered. To mitigate the risk of overfitting and ensure  
 163 model parsimony, a correlation-based feature selection procedure was implemented. We calculated the Pearson cor-

164 relation coefficient between each candidate predictor (e.g., various temperature indices, raw precipitation, vegetation  
 165 metrics) and the target groundwater levels. Variables exhibiting weak correlations ( $|r| < 0.1$ ) or high multicollinearity  
 166 (redundant features) were excluded from the final input set. This process ensured that only the most relevant  
 167 drivers—specifically Precipitation, Adjusted ET, LST, and NDVI—were retained for model training.

168 ***Variable Transformation and Evapotranspiration Partitioning***

169 All predictor variables were resampled to a monthly temporal resolution and temporally aligned with the groundwa-  
 170 ter level observations to ensure consistency between remotely sensed data and in situ measurements. Standard scaling  
 171 was applied where appropriate prior to model training.

172 Evapotranspiration (ET) data were obtained from the FAO WaPOR database and represent total actual evapo-  
 173 transpiration, including both precipitation-driven and groundwater-supported components. To derive a variable more  
 174 directly linked to groundwater availability, the precipitation-driven component of evapotranspiration was estimated  
 175 and removed.

176 Monthly potential evapotranspiration (PET) was computed using the Hargreaves–Samani method [George H. Harg-  
 177 reaves and Zohrab A. Samani \(1985\)](#), a temperature- and radiation-based formulation suitable for data-scarce regions.  
 178 Daily minimum and maximum air temperatures were approximated from land surface temperature (LST) by applying  
 179 a  $\pm 5$  °C offset. Daily PET was estimated as:

$$\text{PET}_d = 0.0023 R_a (T_{\text{mean}} + 17.8) \sqrt{T_{\text{max}} - T_{\text{min}}}, \quad (1)$$

180 where  $T_{\text{mean}}$  is the mean daily air temperature,  $T_{\text{max}}$  and  $T_{\text{min}}$  are the daily maximum and minimum temperatures,  
 181 respectively, and  $R_a$  is the extraterrestrial radiation ( $\text{MJ m}^{-2} \text{ day}^{-1}$ ), computed as a function of latitude and day of year  
 182 following standard formulations. Daily PET estimates were aggregated to monthly totals.

183 The precipitation-driven component of evapotranspiration was estimated using a parametric Budyko framework  
 184 [Budyko \(1974\)](#) based on the Fu formulation [Li et al. \(2022\)](#), which relates evapotranspiration to the ratio between  
 185 potential evapotranspiration and precipitation. The Budyko relationship is expressed as:

$$\frac{ET_{\text{rain}}}{P} = 1 + \frac{PET}{P} - \left( 1 + \left( \frac{PET}{P} \right)^{\omega} \right)^{1/\omega}, \quad (2)$$

186 where  $P$  denotes monthly precipitation,  $PET$  is monthly potential evapotranspiration, and  $\omega$  is a dimensionless  
 187 shape parameter controlling the partitioning behavior. A value of  $\omega = 2.6$  was adopted to represent typical semi-arid

188 climatic conditions. The resulting  $ET_{\text{rain}}$  represents precipitation-driven (rainfed) evapotranspiration.  
 189 Groundwater-dependent evapotranspiration was then estimated as the residual between total actual evapotranspi-  
 190 ration and the precipitation-driven component:

$$ET_{\text{gw}} = ET_{\text{total}} - ET_{\text{rain}}. \quad (3)$$

191 To avoid non-physical estimates, negative values of  $ET_{\text{gw}}$  were constrained to zero. While this approach represents  
 192 a simplified treatment of land–atmosphere and subsurface interactions, it provides a physically motivated proxy for  
 193 groundwater-related evapotranspiration dynamics in the vicinity of the monitored wells.

### 194 2.3. Graph Construction

195 The groundwater monitoring network was modeled as a graph, where nodes represent wells and edges represent  
 196 relationships between them, following approaches commonly used in recent spatio-temporal graph neural network  
 197 (STGNN) frameworks for groundwater prediction Taccari et al. (2024). Several strategies can be adopted to define  
 198 edges in such a graph. A straightforward approach is to use spatial proximity, under the assumption that wells lo-  
 199 cated near each other are likely to share similar hydrogeological conditions; distance-based adjacency using Haversine  
 200 distances and  $k$ -nearest neighbors ( $k$ -NN) is widely adopted in GNN-based groundwater studies Bai and Tahmasebi  
 201 (2023). In this study, pairwise distances between wells were calculated using the Haversine formula, and edges were  
 202 assigned following a  $k$ -NN strategy. This ensures that each well is connected to its closest neighbors, capturing local  
 203 spatial dependencies; similar graph construction strategies are standard in machine learning and spatial modeling Chen  
 204 et al. (2009).

205 Alternative definitions of connectivity are also possible. Hydrogeological similarity can be used when detailed  
 206 subsurface data (e.g., aquifer structure or soil properties) are available, and multi-form spatial dependency models  
 207 combining distance, hydrogeologic attributes, and functional similarity have been proposed Wu et al. (2025). Another  
 208 option is correlation-based connectivity, where wells exhibiting similar groundwater dynamics are connected regard-  
 209 less of spatial distance; such functional graphs have been applied in data-driven hydrogeological studies Wu et al.  
 210 (2025). While these approaches may capture teleconnection patterns more directly, they can also introduce spurious  
 211 or non-physical dependencies and risk temporal data leakage if not restricted to the training window 'CITE'.

212 For the purposes of this study, a distance-based adjacency was adopted as a robust and physically interpretable  
 213 baseline. This choice balances simplicity, hydrogeologic plausibility, and reproducibility in the absence of detailed  
 214 subsurface information, and aligns with existing STGNN groundwater forecasting literature Taccari et al. (2024); Bai  
 215 and Tahmasebi (2023).

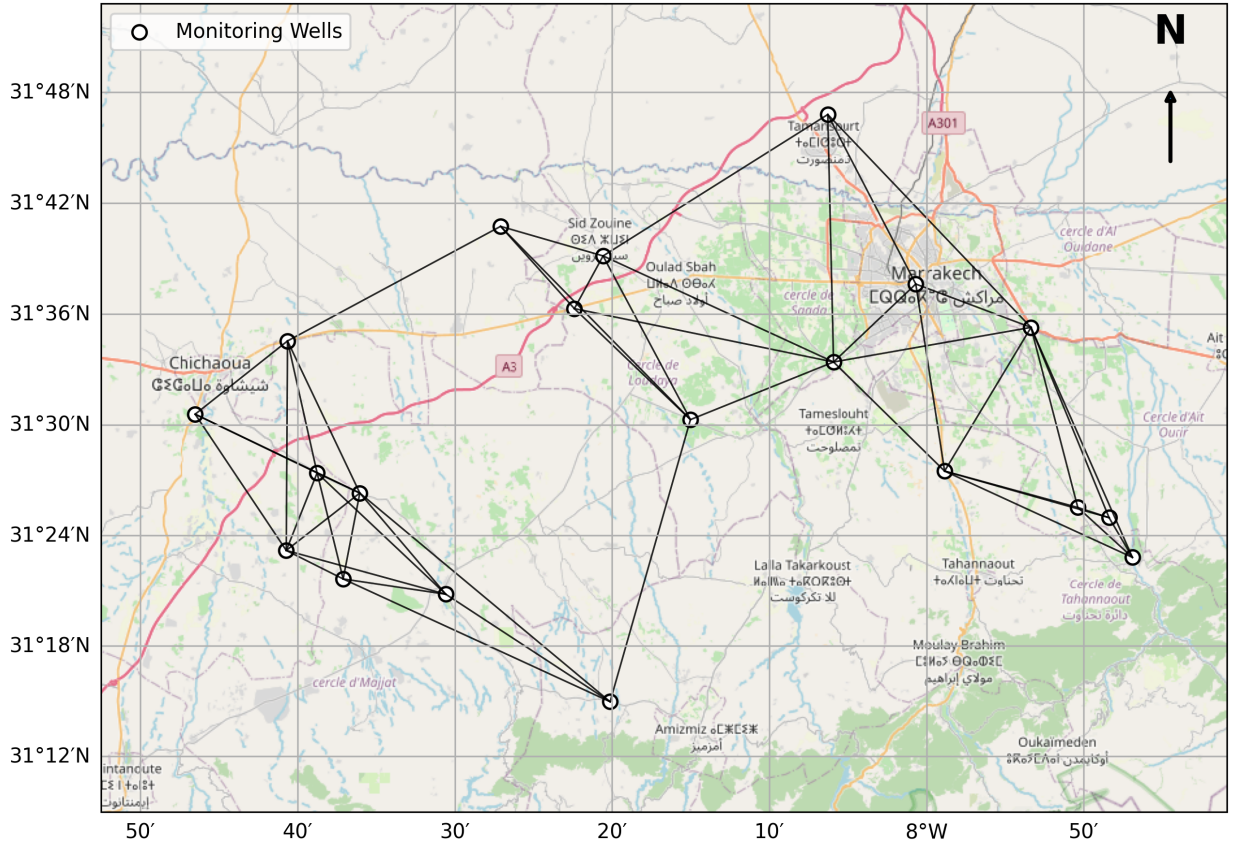


**Figure 4:** Graph representation of the groundwater monitoring network. Nodes correspond to wells, and edges are defined based on spatial proximity using a  $k$ -nearest neighbors ( $k$ -NN) approach with pairwise Haversine distances. This distance-based adjacency captures local spatial dependencies among wells while providing a physically interpretable and reproducible baseline for spatio-temporal graph neural network modeling.

## 216 2.4. Model Architecture

### 217 2.4.1. Graph Neural Networks (GNNs)

218 Graph Neural Networks (GNNs) extend deep learning methods to graph-structured data, where the relationships  
 219 between nodes are as important as the attributes of the nodes themselves. The core principle of GNNs is *message*  
 220 *passing*, formalized in early works on neural networks for graphs and later generalized in the Message Passing Neural  
 221 Network (MPNN) framework Kipf and Welling (2017); Gilmer et al. (2017). At each layer, every node aggregates  
 222 features from its neighbors and updates its own representation.

223 Formally, let a graph be defined as  $G = (V, E)$ , where  $V$  is the set of nodes (wells) and  $E$  the set of edges. For a  
 224 node  $v \in V$ , the update rule in a generic GNN layer can be written as:

$$h_v^{(l+1)} = \sigma\left(W^{(l)} \cdot \text{AGG}\left(\{h_u^{(l)} : u \in \mathcal{N}(v)\} \cup \{h_v^{(l)}\}\right)\right), \quad (4)$$

225 where  $h_v^{(l)}$  is the representation of node  $v$  at layer  $l$ ,  $\mathcal{N}(v)$  denotes the neighborhood of  $v$ ,  $W^{(l)}$  is a learnable weight  
 226 matrix, and  $\sigma$  is a non-linear activation. The function AGG is a permutation-invariant aggregator (mean, sum, or max),  
 227 as established in the MPNN formulation Gilmer et al. (2017).

#### 228 2.4.2. Graph Convolutional Networks (GCNs)

229 The Graph Convolutional Network (GCN) is a specific type of GNN that simplifies the message passing scheme  
 230 using a normalized adjacency matrix. The spectral GCN formulation used in most applications was popularized by  
 231 Kipf and Welling Kipf and Welling (2017). Given feature matrix  $X \in \mathbb{R}^{N \times d}$  and adjacency matrix  $A \in \mathbb{R}^{N \times N}$ , the  
 232 forward propagation of a GCN layer is:

$$H^{(l+1)} = \sigma(\tilde{D}^{-\frac{1}{2}} \tilde{A} \tilde{D}^{-\frac{1}{2}} H^{(l)} W^{(l)}), \quad (5)$$

233 where  $\tilde{A} = A + I$  is the adjacency matrix with self-loops,  $\tilde{D}$  is the diagonal degree matrix of  $\tilde{A}$ ,  $H^{(0)} = X$  is the input  
 234 feature matrix,  $W^{(l)}$  are learnable weights, and  $\sigma$  is a non-linear activation. This formulation ensures that each node  
 235 updates its representation as a weighted average of its neighbors' features, normalized to avoid scale issues Kipf and  
 236 Welling (2017).

#### 237 2.4.3. Spatio-Temporal Graph Convolutional Networks (STGCNs)

238 Groundwater levels exhibit both temporal dependencies (fluctuations over time) and spatial dependencies (inter-  
 239 actions among wells influenced by hydrogeological conditions). The STGCN integrates temporal and spatial modules  
 240 into a unified framework, introduced originally for traffic forecasting by Yu et al. (2018) and later applied to environ-  
 241 mental and hydrological systems Taccari et al. (2024).

242 Each spatio-temporal block consists of:

243 1. **Temporal convolution:** For an input sequence  $X \in \mathbb{R}^{N \times F \times T}$ , a 1D convolution is applied along the temporal  
 244 axis:

$$Z = \text{Conv1D}_{\text{time}}(X), \quad (6)$$

245 as proposed in temporal convolutional architectures such as STGCN Yu et al. (2018).

246 2. **Graph convolution:** At each time step, spatial dependencies are captured using the GCN operation:

$$H_t^{(l+1)} = \sigma(\tilde{D}_t^{-\frac{1}{2}} \tilde{A}_t \tilde{D}_t^{-\frac{1}{2}} H_t^{(l)} W^{(l)}), \quad \forall t \in [1, T], \quad (7)$$

247 which follows the spectral GCN formulation Kipf and Welling (2017).

248     **3. Residual connections and normalization:** These stabilize learning and allow deeper stacking, as adopted in  
 249     STGCN and related spatio-temporal architectures Yu et al. (2018).

250     Stacking multiple spatio-temporal blocks results in a deep encoder-like structure, followed by fully connected layers  
 251     to predict future groundwater levels, consistent with recent applications in hydrology Taccari et al. (2024).

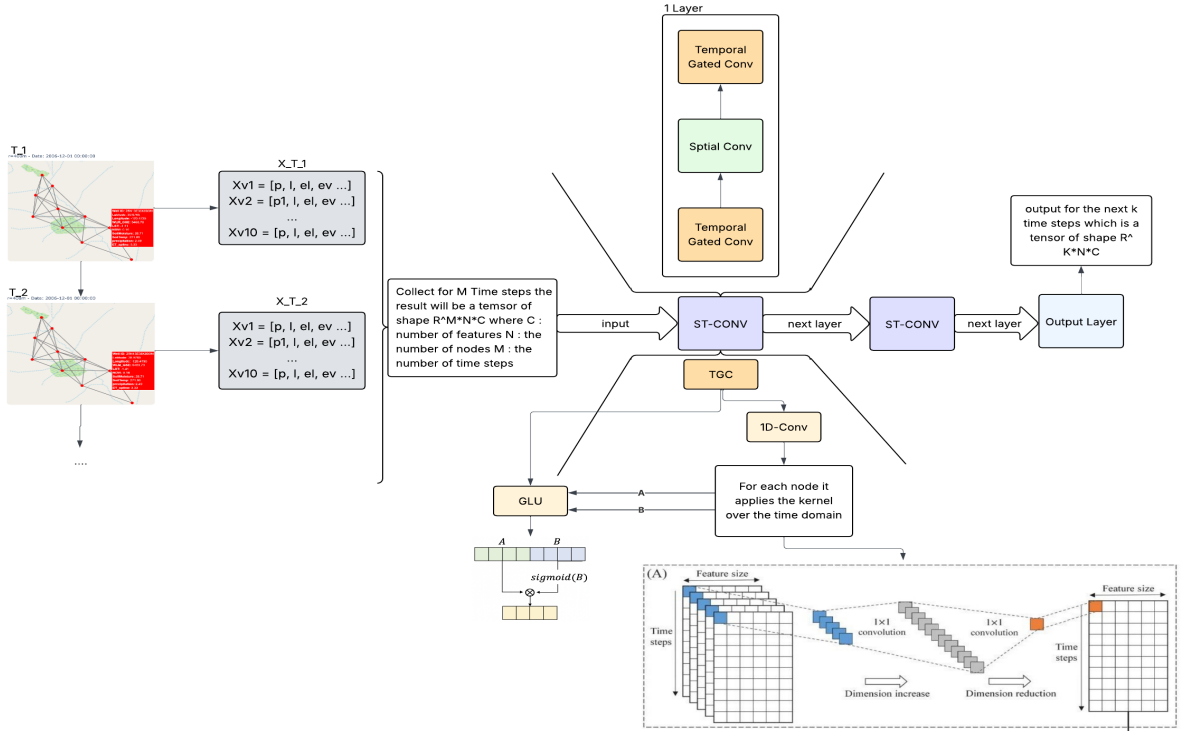


**Figure 5:** Architecture of the Spatio-Temporal Graph Convolutional Network (STGNN) used in this study. The model stacks multiple spatio-temporal blocks to capture spatial and temporal dependencies in groundwater data, followed by fully connected layers for forecasting future groundwater levels, consistent with recent hydrological applications Taccari et al. (2024).

## 252     2.5. Training and Evaluation

253     The model was trained to learn the complex spatio-temporal dependencies governing groundwater level (GWL)  
 254     dynamics across the wells. Each training sample consists of a sequence of past groundwater levels and corresponding  
 255     features (e.g., precipitation, evapotranspiration, temperature), and the target is the GWL value at the next time step (or  
 256     multiple future steps for multi-step forecasting).

### 257     Training Procedure

258     The dataset was divided into training, validation, and testing subsets. The model was trained for a fixed number of  
 259     epochs using the Adam optimizer, with a learning rate scheduler to improve convergence stability.

260 The forward pass produces predicted groundwater levels  $\hat{y}_t$  for each node and time step, and the parameters of the  
 261 model are updated by minimizing the loss function between the predicted and observed values  $y_t$ .

262 The loss function used is the **Mean Squared Error (MSE)**, defined as:

$$\mathcal{L}_{\text{MSE}} = \frac{1}{NT} \sum_{i=1}^N \sum_{t=1}^T (y_{i,t} - \hat{y}_{i,t})^2 \quad (8)$$

263 where:  $N$  is the number of wells (graph nodes),  $T$  is the number of time steps,  $y_{i,t}$  is the observed groundwater  
 264 level for well  $i$  at time  $t$ ,  $\hat{y}_{i,t}$  is the model's prediction.

265 This loss penalizes larger errors more heavily, encouraging the model to focus on capturing extreme variations in  
 266 groundwater levels.

267 The training and validation losses across epochs are shown in Figure 6. The gradual convergence of both losses  
 268 indicates that the model successfully generalizes without overfitting.

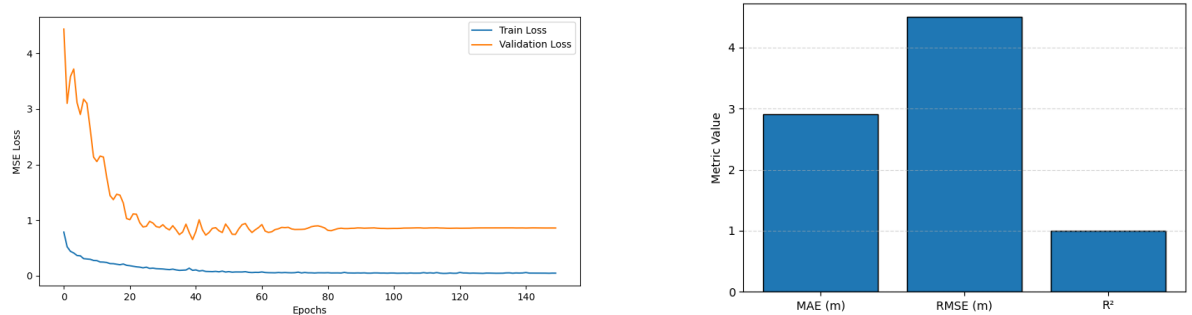


**Figure 6:** Overview of model performance. (a) Training and validation loss across epochs, showing gradual convergence and indicating effective generalization without overfitting. (b) Evaluation metrics on the test set, illustrating the model's accuracy in capturing groundwater level dynamics and its sensitivity to extreme variations.

### 269 2.5.1. Evaluation Metrics

270 The model performance was evaluated on the test set using three complementary metrics to capture different aspects  
 271 of prediction quality:

- 272 • **Mean Absolute Error (MAE)** measures the average magnitude of errors:

$$\text{MAE} = \frac{1}{NT} \sum_{i=1}^N \sum_{t=1}^T |y_{i,t} - \hat{y}_{i,t}| \quad (9)$$

273

- Root Mean Square Error (RMSE) emphasizes larger errors, providing insight into extreme deviations:

$$\text{RMSE} = \sqrt{\frac{1}{NT} \sum_{i=1}^N \sum_{t=1}^T (y_{i,t} - \hat{y}_{i,t})^2} \quad (10)$$

274

- Coefficient of Determination ( $R^2$ ) measures how well the predictions explain the variance in the observed data:

275

$$R^2 = 1 - \frac{\sum_{i,t} (y_{i,t} - \hat{y}_{i,t})^2}{\sum_{i,t} (y_{i,t} - \bar{y})^2} \quad (11)$$

276

where  $\bar{y}$  is the mean of the observed values.

277

Higher  $R^2$  values (close to 1) and lower MAE/RMSE indicate better forecasting performance.

278

Overall, these results provide quantitative evidence that the STGCN model effectively captures both temporal patterns and spatial dependencies in groundwater level dynamics.

280

## 2.6. Baseline Models

281

For the baseline models, LSTM and GRU architectures were used due to their proven effectiveness in time-series prediction tasks. The comparison results show that the STGCN generally provides more accurate predictions over time. However, this improvement is not consistent across all wells, which can be attributed to the heterogeneity and complexity of the data. For wells with more regular temporal patterns, the baseline models perform slightly better than the STGCN. Nevertheless, our focus is on the challenging, irregular cases where the STGCN demonstrates its advantage.

Model	MAE (m)	RMSE (m)	$R^2$
STGNN	2.9022	4.4968	0.9994
LSTM	2.9929	5.2329	0.9991
GRU	3.7084	6.2149	0.9988

**Table 1**

Comparison of model performance in groundwater level prediction. Metrics include mean absolute error (MAE), root mean squared error (RMSE), and coefficient of determination ( $R^2$ ). The STGCN generally outperforms LSTM and GRU models, particularly for wells with irregular temporal patterns, highlighting its ability to capture complex spatio-temporal dependencies.

287

**Analysis of Aggregate Performance :** Figure 7 highlights the aggregate performance gap between the proposed STGCN and the recurrent baselines (LSTM and GRU). The STGCN (blue bars) achieves the lowest error rates across the board, reducing the RMSE by approximately 14% compared to the LSTM and 27% compared to the GRU. The  $R^2$  metric further corroborates this, with the graph-based model maintaining a near-perfect global fit ( $> 0.99$ ), whereas the

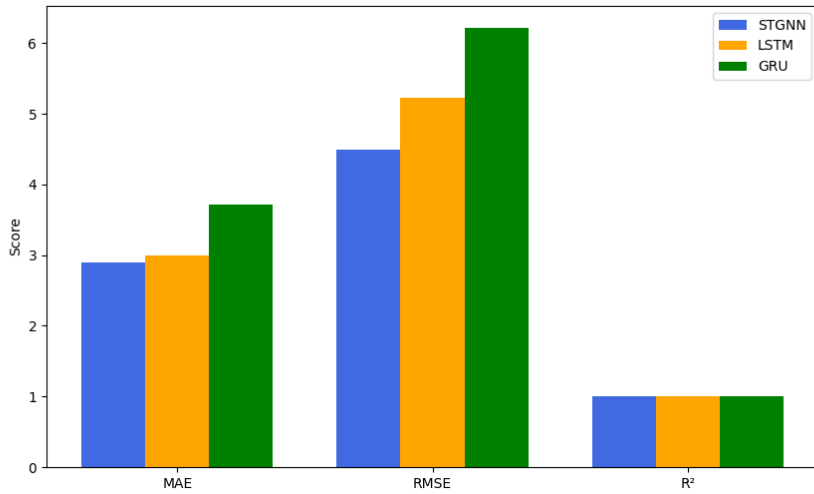


**Figure 7:** Metrics comparison of the two baseline models (LSTM and GRU) with the STGNN model.

291 GRU struggles to capture the variance in the dataset. This suggests that while recurrent units are capable of modeling  
 292 temporal sequences, they fail to leverage the spatial information that stabilizes predictions in a regional aquifer system.

293 **Well-Specific Performance Heterogeneity :** Table 2 provides a granular breakdown of performance, revealing an  
 294 important distinction in model behavior. While the STGCN outperforms baselines in the majority of wells, there are  
 295 specific instances (e.g., Well 766/53 and Well 3595/53) where the LSTM achieves marginally higher  $R^2$  scores. These  
 296 exceptions generally occur in wells exhibiting highly localized behavior or those located at the aquifer's periphery,  
 297 where spatial neighbor connections may be less informative. However, in critical wells with complex dynamics and  
 298 high variability (such as Well 2009/52 and Well 4123/53), the STGCN demonstrates superior robustness, significantly  
 299 mitigating the extreme negative  $R^2$  values observed in the baseline models. This indicates that the graph structure  
 300 effectively acts as a regularizer, preventing the massive prediction errors that isolated time-series models are prone to  
 301 during volatile periods.

Well	STGNN			LSTM			GRU		
	MAE	RMSE	R <sup>2</sup>	MAE	RMSE	R <sup>2</sup>	MAE	RMSE	R <sup>2</sup>
766/53	0.8665	1.1158	0.4055	<b>0.7510</b>	<b>0.9139</b>	<b>0.6011</b>	0.9550	1.0998	0.4223
4442/44	1.8359	2.0590	-21.3732	<b>0.8750</b>	<b>1.0113</b>	<b>-4.3980</b>	1.6207	1.8058	-16.2102
4406/44	1.5358	1.9704	-0.2581	<b>0.7454</b>	1.2240	0.5145	<b>0.7290</b>	<b>1.2146</b>	<b>0.5220</b>
4405/44	0.4545	0.6071	-1.9435	<b>0.2223</b>	<b>0.3789</b>	<b>-0.1466</b>	0.4186	0.5395	-1.3246
4364/44	2.2890	2.4086	-16.6905	<b>2.1384</b>	<b>2.2168</b>	<b>-13.9858</b>	2.6081	2.6380	-20.2208
4010/53	<b>2.9373</b>	<b>3.1758</b>	<b>-5.1524</b>	3.1319	3.3357	-5.7877	4.0897	4.2436	-9.9855
3976/53	2.5702	2.7680	-1.7261	<b>0.7270</b>	<b>0.9496</b>	<b>0.6791</b>	0.9775	1.1862	0.4993
3850/53	0.8655	0.9802	-4.7492	<b>0.7026</b>	<b>0.8378</b>	<b>-3.1998</b>	0.9689	1.1178	-6.4766
3848/53	0.9689	1.4465	-1.4433	0.5632	0.6950	0.4360	<b>0.4095</b>	<b>0.5556</b>	<b>0.6396</b>
3595/53	3.5369	4.0585	-0.3420	<b>2.7094</b>	<b>3.0312</b>	<b>0.2514</b>	3.9927	4.2385	-0.4637
2826/53	1.2117	1.6496	-7.4196	<b>1.1774</b>	<b>1.2174</b>	<b>-3.5857</b>	1.5095	1.5915	-6.8373
2122/52	0.9623	1.3955	-1.8567	<b>0.7014</b>	1.0147	<b>-0.5105</b>	1.1232	<b>1.3621</b>	-1.7217
2701/53	0.9972	1.4371	-0.6562	<b>0.5161</b>	<b>0.6364</b>	<b>0.6752</b>	0.5061	0.6429	0.6686
2700/53	1.4206	1.7508	-6.7185	<b>0.8646</b>	<b>0.9750</b>	<b>-1.3935</b>	1.2645	1.4619	-4.3811
2698/53	0.7377	0.8827	-0.0226	<b>0.2892</b>	<b>0.3606</b>	<b>0.8294</b>	0.3709	0.4216	0.7667
2009/52	<b>12.5478</b>	<b>13.2876</b>	<b>-9.1205</b>	16.6293	17.1444	-15.8483	18.9665	19.3803	-20.5292
2008/52	<b>7.7916</b>	<b>8.5157</b>	<b>-569.1771</b>	9.7309	9.8571	-762.9545	13.3363	13.4321	-1417.5862
1886/52	<b>2.8002</b>	<b>3.1453</b>	<b>-2.4510</b>	4.5317	4.8088	-7.0668	5.0457	5.2322	-8.5496
4123/53	<b>3.8988</b>	<b>4.1425</b>	-15.4744	4.0058	4.1366	<b>-15.4270</b>	5.5304	5.5917	-29.0167
1133/52	<b>7.8165</b>	<b>8.0567</b>	<b>-16.9498</b>	8.8452	9.0294	-21.5454	9.7452	9.9290	-26.2616

**Table 2**

Per-well performance comparison for STGNN, LSTM, and GRU models. Best values per metric (MAE, RMSE, R<sup>2</sup>) are highlighted in bold.

### 3. Results and Discussion

The proposed Spatio-Temporal Graph Convolutional Network (STGCN) demonstrated strong predictive capabilities for groundwater level (GWL) forecasting across the study area. Figure 8 shows a visual comparison between the observed and predicted groundwater levels during both training and testing periods. The close alignment between the two indicates that the model effectively captures the long-term trends and short-term fluctuations of GWL dynamics.

**Temporal Dynamics and Generalization :** Figure 8 presents the hydrographs for three representative monitoring wells, delineating the training, validation, and testing phases. A visual inspection reveals the model's ability to track disparate hydrological regimes:

- Trend Capture:** In Well 4442/44 (Top Panel), the STGCN accurately reproduces the seasonal cyclicity while adhering to the gradual recovery trend observed in the validation phase.

- Response to Abrupt Changes:** Well 4406/44 (Middle Panel) exhibits a sharp drawdown event during the testing phase (right of the purple vertical line). Unlike standard regression models that often suffer from lag or smoothing, the STGCN anticipates this drop, attributed to its ability to aggregate information from neighboring wells that may have experienced the stress earlier.

- Handling Noise:** Well 4405/44 (Bottom Panel) represents a high-frequency fluctuation scenario. The model

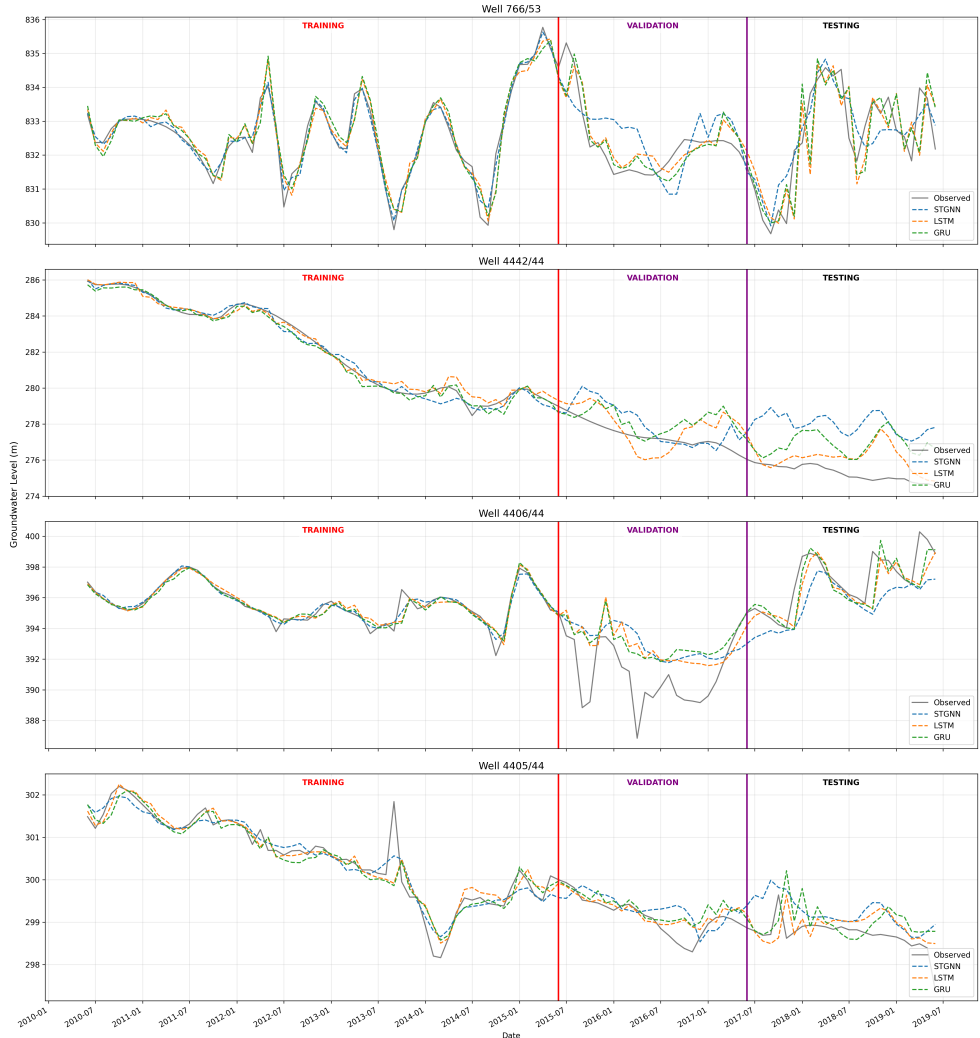
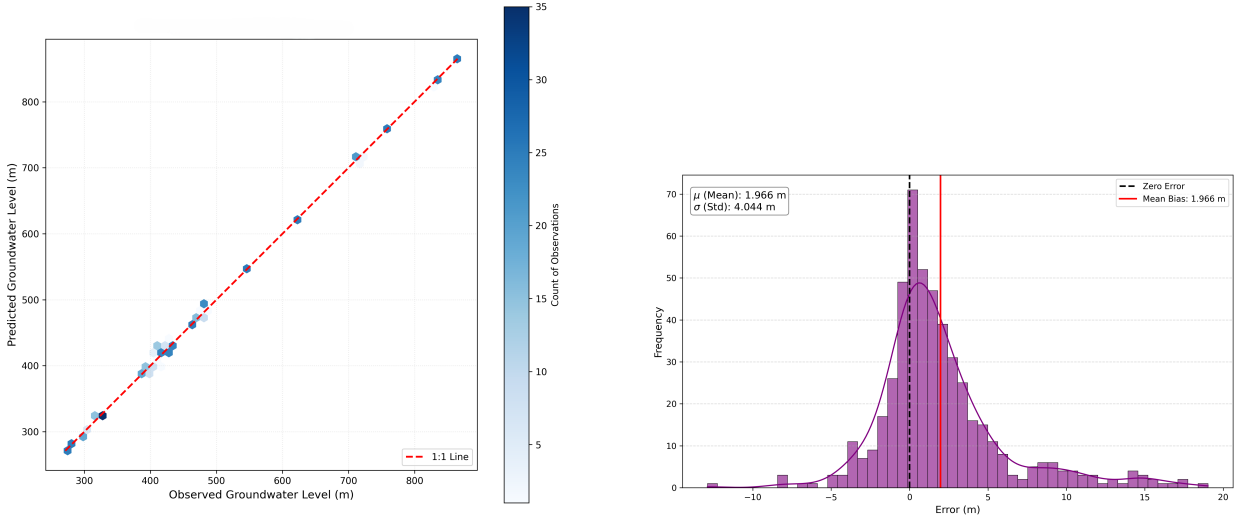


**Figure 8:** Comparison of observed and predicted groundwater levels for the training and testing periods. The close alignment illustrates the STGCN's ability to accurately capture both long-term trends and short-term fluctuations in groundwater dynamics.

317 predictions (orange dashed line) tightly hug the observed data (grey line), indicating that the model successfully  
318 disentangles signal from noise without overfitting to the training data.

319 The close alignment in the testing phase confirms that the model does not merely memorize historical sequences but  
320 generalizes well to unseen climatic and hydrological conditions.

321 **Error Distribution and Goodness-of-Fit :** To further assess the reliability of the forecasts, we analyzed the statistical  
322 properties of the residuals. Figure 9a displays the scatter plot of observed versus predicted groundwater levels. The  
323 data points cluster tightly around the 1:1 diagonal line (red dashed), indicating a lack of systematic bias across the  
324 range of groundwater depths. There is no significant deviation at the tails, suggesting the model performs equally well



(a) Observed vs predicted groundwater levels

(b) STGNN: Distribution of Residuals.

**Figure 9:** Evaluation of STGCN prediction performance. (a) Scatter plot of observed versus predicted groundwater levels, demonstrating strong agreement and model generalization to unseen conditions. (b) Distribution of residuals across all wells, highlighting the model's error characteristics and overall prediction reliability.

325 for both shallow and deep water tables.

326 Figure 9b illustrates the distribution of prediction residuals. The error histogram approximates a Gaussian (normal)  
 327 distribution centered near zero ( $\mu \approx 1.96$  m), with a controlled standard deviation. The symmetry of the bell curve  
 328 indicates that the model is not biased toward overestimation or underestimation. The slight positive mean bias suggests  
 329 a very marginal tendency to under-predict drawdown in extreme cases, likely due to the inherent smoothing effect of  
 330 the graph convolution operator, yet the majority of errors fall within an acceptable range for regional management  
 331 planning.

### 332 3.1. Model Performance and Interpretation

333 The evaluation metrics (MAE, RMSE, and  $R^2$ ) revealed that the STGCN achieved high accuracy and stable gener-  
 334 alization across the different wells. The model outperformed baseline approaches such as classical LSTMs, particularly  
 335 during periods of high variability (e.g., seasonal transitions). This improvement is consistent with findings from related  
 336 studies, where STGNN-based methods reduced forecasting errors by approximately 15–20% compared to sequence-  
 337 only models.

338 **Drivers of Groundwater Dynamics :** To understand the physical drivers influencing the STGCN's predictions, we  
 339 conducted a permutation feature importance analysis (Figure 10a). The results identify `et_groundwater` (evapotran-  
 340 spiration adjusted via the Budyko framework) as the single most influential predictor. This aligns with the hydrogeo-  
 341 logical reality of the Haouz region, where groundwater depletion is primarily driven by irrigation demands rather than

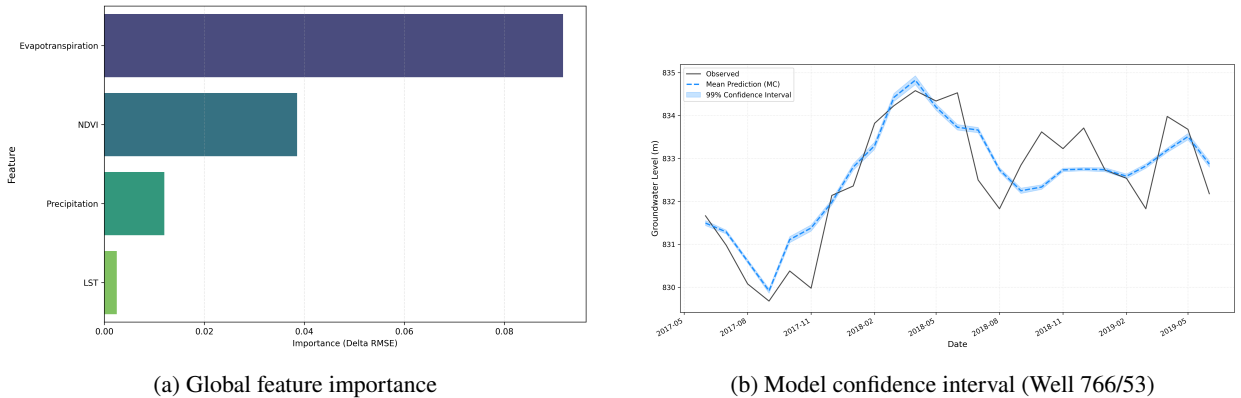


**Figure 10:** Model interpretability and reliability. (a) Global feature importance across all wells, showing which inputs most strongly influence STGCN predictions. (b) Prediction confidence intervals for well 766/53, illustrating the model's uncertainty and robustness during periods of high groundwater variability.

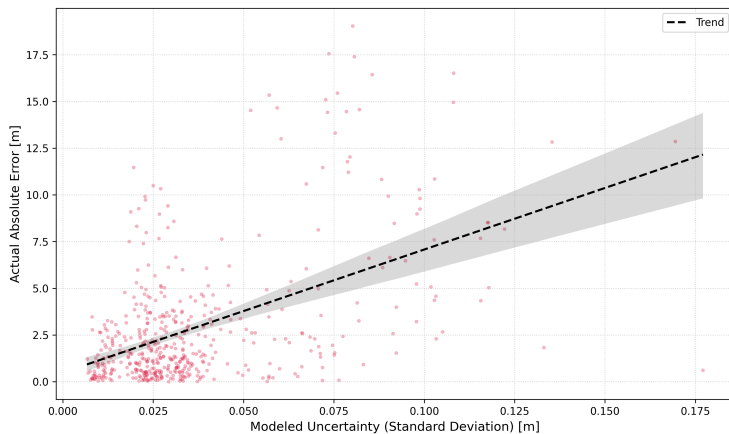


**Figure 11:** Relationship between predicted uncertainty and actual prediction error. The scatter plot shows that higher modeled uncertainty (standard deviation of predictions) corresponds to larger absolute errors, indicating that the STGCN's uncertainty estimates are well-calibrated and can serve as a reliable proxy for risk in groundwater management decisions.

342 natural fluctuations.

343 Interestingly, Precipitation exhibits a lower importance score relative to Land Surface Temperature (LST) and  
344 NDVI. This suggests that the aquifer's response to rainfall is highly non-linear and lagged (due to the infiltration process  
345 through the vadose zone), whereas variables like LST and NDVI serve as immediate proxies for evaporative stress and  
346 agricultural water withdrawal.

347 **Uncertainty Calibration :** Figure 11 validates the reliability of the model's uncertainty estimates. The scatter plot  
348 illustrates the relationship between the modeled uncertainty (standard deviation of the prediction distribution) and the  
349 Actual Absolute Error. The distinct positive trend, highlighted by the regression line, demonstrates that the model is  
350 well-calibrated: as the predicted uncertainty increases, the likelihood of a larger error also increases.

351 For decision-makers, this linear relationship is valuable. It implies that the uncertainty metric output by the STGCN

352 can be used as a trustworthy proxy for risk. If the model predicts a groundwater level with a high uncertainty variance,  
 353 water managers can prioritize those specific wells for manual verification or additional sensor deployment, thereby  
 354 optimizing monitoring resources.

### 355 3.2. Effect of Spatial Relationships

356 Using spatial proximity as the basis for the graph structure proved effective in capturing coherent spatial patterns  
 357 in groundwater dynamics. However, wells influenced by anthropogenic factors (e.g., pumping, irrigation) or localized  
 358 hydrogeological differences exhibited deviations from purely distance-based similarity. Future work could benefit  
 359 from incorporating more physically meaningful relationships, such as hydraulic conductivity, lithology, or correlation  
 360 in groundwater dynamics, to refine the graph construction.

361 **Spatial Distribution of Error and Uncertainty :** To assess the reliability of the STGCN across the heterogeneous  
 362 landscape of the Haouz aquifer, we visualized the spatial distribution of model performance in Figure 12. In this  
 363 diagnostics map, the color scale represents the prediction error (RMSE), while the size of the markers is proportional  
 364 to the model's predictive uncertainty (confidence interval width).

365 The map reveals a dominant prevalence of blue markers, indicating low RMSE values across the majority of the  
 366 monitoring network. This confirms the model's capability to generalize well over spatially disjoint locations. How-  
 367 ever, distinct clusters of larger, red-hued nodes are observable, particularly in zones known for intensive agricultural  
 368 activity. The correlation between marker size and color intensity is notable: wells where the model exhibits high  
 369 prediction error often coincide with high uncertainty estimates. This "self-awareness" of the model is a critical safety  
 370 feature; it indicates that the STGCN can flag its own limitations in areas with complex, non-stationary dynamics driven  
 371 by unmeasured anthropogenic factors (e.g., unreported illegal pumping), rather than making confident but incorrect  
 372 predictions.

### 373 3.3. Temporal Dynamics and Seasonal Variability

374 The STGCN successfully reproduced seasonal oscillations associated with precipitation and evapotranspiration  
 375 cycles, as well as gradual long-term declines in wells affected by persistent overextraction. However, during abrupt  
 376 hydrological events (e.g., extreme drought or heavy rainfall), the model exhibited slightly higher prediction errors.  
 377 This suggests that while STGCNs can capture regular spatio-temporal dependencies effectively, additional external  
 378 drivers (e.g., surface water–groundwater interactions or land use changes) could further enhance forecasting accuracy.

### 379 3.4. Interpretability and Practical Insights

380 In addition to its predictive power, the model provides interpretability benefits. Attention-based graph variants of  
 381 the STGCN can quantify the relative influence of neighboring wells, revealing which monitoring sites exert the most

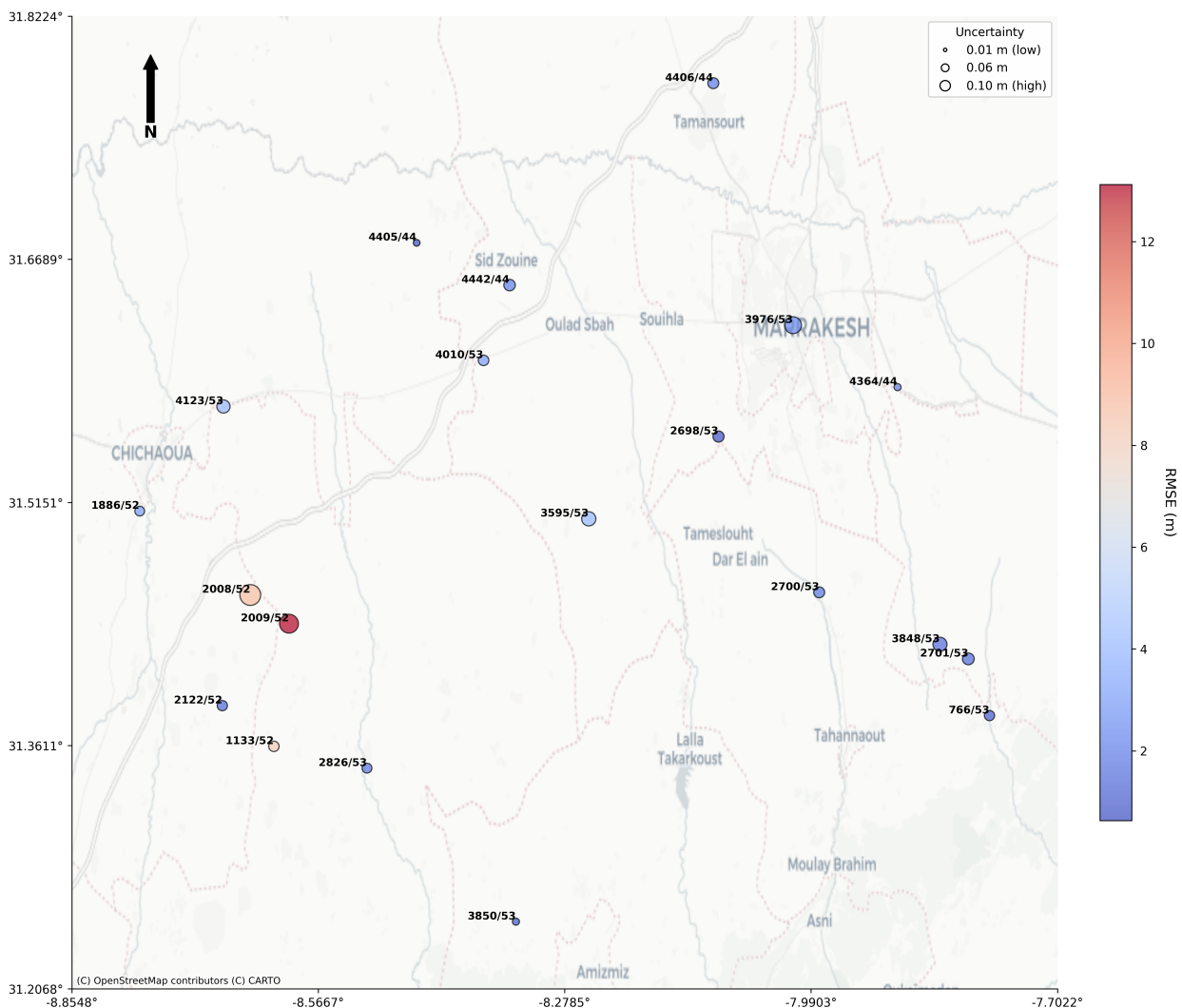


**Figure 12:** Spatial diagnostics of STGCN performance across the monitoring network. Node color represents prediction accuracy, while node size indicates model confidence. This visualization highlights wells where anthropogenic activities or local hydrogeological heterogeneity lead to deviations from the distance-based graph assumptions, providing insights for targeted model refinement and monitoring prioritization.

382 significant impact on regional groundwater dynamics. Such insights can assist decision-makers in:

- 383 • Optimizing the placement of monitoring wells,
- 384 • Identifying critical aquifer zones vulnerable to depletion,
- 385 • Supporting sustainable groundwater management under changing climatic and anthropogenic pressures.

386 Overall, the results demonstrate that the proposed framework captures both the spatial and temporal characteristics  
 387 of groundwater systems, outperforming purely temporal or statistical approaches and offering new opportunities for  
 388 data-driven water resource modeling.

389 **4. Conclusion**

390 This study presented a novel application of Spatio-Temporal Graph Neural Networks (STGNNs) for regional  
 391 groundwater level forecasting in the semi-arid Haouz Aquifer, Morocco. By conceptualizing the monitoring network as  
 392 a dynamic graph, we successfully integrated spatial dependencies—representing hydraulic connectivity—with tempo-  
 393 ral hydrological sequences. This approach addressed a critical methodological gap in standard deep learning models  
 394 (such as LSTM and GRU), which treat monitoring wells as isolated entities and often fail to capture the systemic  
 395 response of the aquifer to anthropogenic and climatic stressors.

396 The empirical results demonstrate that the proposed STGNN framework significantly outperforms baseline tem-  
 397 poral models, reducing the Root Mean Square Error (RMSE) by approximately 14% compared to the LSTM and 27%  
 398 compared to the GRU. The model exhibited remarkable robustness, maintaining high predictive accuracy ( $R^2 > 0.99$ )  
 399 even in wells characterized by irregular fluctuations and sharp seasonal drawdowns. Furthermore, the inclusion of  
 400 uncertainty quantification revealed a strong correlation between predicted uncertainty and actual error, establishing  
 401 the model as a reliable decision-support tool for identifying high-risk areas in data-scarce regions. Ultimately, this  
 402 research confirms that explicit modeling of spatial interactions is a prerequisite for accurate groundwater forecasting  
 403 in complex, over-exploited aquifer systems.

404 **5. Future Work**

405 While the proposed STGNN framework offers a robust data-driven solution, several avenues remain for further  
 406 enhancement, particularly regarding the physical consistency of predictions and long-term scenario planning.

407 **5.1. Integration of Physics-Informed Neural Networks (PINNs)**

408 A primary direction for future research is to bridge the gap between data-driven efficiency and physical realism  
 409 by incorporating Physics-Informed Neural Networks (PINNs). While STGNNs effectively learn statistical spatio-  
 410 temporal patterns, they do not explicitly enforce fundamental hydrogeological laws, such as the conservation of mass  
 411 or Darcy's Law. Consequently, purely data-driven models may occasionally produce physically inconsistent predictions  
 412 in unmonitored locations.

413 Future iterations of this work aim to embed these governing partial differential equations (PDEs) directly into  
 414 the network's loss function. A hybrid architecture combining STGNNs with PINNs would ensure that predictions  
 415 remain hydrogeologically plausible, effectively acting as a regularization mechanism. This approach is expected to  
 416 significantly improve performance in data-scarce zones and enhance the model's ability to generalize during extreme  
 417 climatic events where historical training data is insufficient.

**418 5.2. Dynamic and Functional Graph Construction**

419 The current study utilized distance-based adjacency to define the graph structure. However, hydraulic connectivity  
420 is not solely a function of geometric distance but is also influenced by subsurface heterogeneity, geological faults, and  
421 transmissivity. Future work could explore learning the graph structure dynamically from data (adaptive adjacency  
422 matrices) or constructing graphs based on functional similarity and geological surveys to better represent the physical  
423 flow paths within the aquifer.

**424 5.3. Climate Change and Scenario Analysis**

425 Finally, to support long-term sustainable management, the framework should be extended to simulate future ground-  
426 water trajectories under various CMIP6 climate change scenarios and socioeconomic abstraction pathways. Integrating  
427 these long-term projections will transform the model from a short-term forecasting tool into a comprehensive platform  
428 for strategic water resource planning in the Tensift basin.

**429 6. Acknowledgments**

430 **Code availability section**

431 Name of the code/library

432 Contact: and phone number

433 Hardware requirements: ...

434 Program language: ...

435 Software required: ...

436 Program size: ...

437 The source codes are available for downloading at the link: [https://github.com/ . . . .](https://github.com/)438 **References**

- 439 Anderson, M.P., Hunt, R.J., Woessner, W.W., 2015. Applied groundwater modeling: simulation of flow and advective transport. Second edition  
440 ed., Academic Press, London, UK.
- 441 Bai, T., Tahmasebi, P., 2023. Graph neural network for groundwater level forecasting. Journal of Hydrology 616, 128792. URL: <https://www.sciencedirect.com/science/article/pii/S0022169422013622>, doi:10.1016/j.jhydrol.2022.128792.
- 442 Borzì, I., 2025. Modeling Groundwater Resources in Data-Scarce Regions for Sustainable Management: Methodologies and Limits. Hydrology  
443 12, 11. URL: <https://www.mdpi.com/2306-5338/12/1/11>, doi:10.3390/hydrology12010011. publisher: Multidisciplinary Digital  
444 Publishing Institute.
- 445 Bouramtane, T., Mohsine, I., Karmouda, N., Leblanc, M., Estève, Y., Kacimi, I., Hilali, M., Mdhaffar, S., Tweed, S., Tahir, M., Kassou, N., El Bilali,  
446 A., Chafki, O., 2025. Dimensionality reduction for groundwater forecasting under drought and intensive irrigation with neural networks. Journal  
447 of Hydrology: Regional Studies 60, 102477. URL: <https://www.sciencedirect.com/science/article/pii/S2214581825003027>,  
448 doi:10.1016/j.ejrh.2025.102477.
- 449 Budyko, M.I., 1974. Climate and life [by] M. I. Budyko. Edited by David H. Miller. International geophysics series ; v. 18., Academic Press, New  
450 York.
- 451 Chang, Y.W., Sun, W., Kow, P.Y., Lee, M.H., Chang, L.C., Chang, F.J., 2025. Advanced groundwater level forecasting with hybrid deep learning  
452 model: Tackling water challenges in Taiwan's largest alluvial fan. Journal of Hydrology 655, 132887. URL: <https://www.sciencedirect.com/science/article/pii/S0022169425002252>, doi:10.1016/j.jhydrol.2025.132887.
- 453 Chen, J., Fang, H.r., Saad, Y., 2009. Fast Approximate kNN Graph Construction for High Dimensional Data via Recursive Lanczos Bisection. J.  
454 Mach. Learn. Res. 10, 1989–2012.
- 455 Chen, L., Zhang, D., Xu, J., Zhou, Z., Jin, J., Luan, J., Wulamu, A., 2025. Enhancing the accuracy of groundwater level prediction at dif-  
456 ferent scales using spatio-temporal graph convolutional model. Earth Science Informatics 18, 250. URL: <https://doi.org/10.1007/s12145-025-01741-z>, doi:10.1007/s12145-025-01741-z.
- 457 Didan, K., 2021. Modis/terra vegetation indices 16-day l3 global 1km sin grid v061. NASA Land Processes Distributed Active Archive Center.  
458 URL: <https://doi.org/10.5067/MODIS/MOD13A2.061>, doi:10.5067/MODIS/MOD13A2.061. data set. Accessed: 2025-12-11.
- 459 El Mezouary, L., Hadri, A., Kharrou, M.H., Fakir, Y., Elfarchouni, A., Bouchaou, L., Chehbouni, A., 2024. Contribution to advancing aquifer  
460 geometric mapping using machine learning and deep learning techniques: a case study of the AL Haouz-Mejjate aquifer, Marrakech, Morocco.  
461 Applied Water Science 14, 102. URL: <https://doi.org/10.1007/s13201-024-02162-x>, doi:10.1007/s13201-024-02162-x.

- 465 Elmotawakkil, A., Enneya, N., 2024. Advanced machine learning for predicting groundwater decline and drought in the Rabat–Salé–Kénitra region,  
466 Morocco. *Journal of Hydroinformatics* 26, 2980–3007. URL: <https://doi.org/10.2166/hydro.2024.328>, doi:10.2166/hydro.2024.328.
- 467
- 468 Famiglietti, J.S., 2014. The global groundwater crisis. *Nature Climate Change* 4, 945–948. URL: <https://www.nature.com/articles/nclimate2425>, doi:10.1038/nclimate2425. publisher: Nature Publishing Group.
- 469
- 470 Food and Agriculture Organization of the United Nations (FAO), 2020. WaPOR V2 Database Methodology. Technical Report. FAO. Rome. URL:  
471 <https://www.fao.org/3/ca9894en/CA9894EN.pdf>.
- 472 Funk, C., Peterson, P., Landsfeld, M., Pedreros, D., Verdin, J., Shukla, S., Husak, G., Rowland, J., Harrison, L., Hoell, A., Michaelsen, J., 2015. The  
473 climate hazards infrared precipitation with stations (chirps): A new environmental record for monitoring extremes. *Scientific Data* 2, 150066.  
474 doi:10.1038/sdata.2015.66.
- 475 George H. Hargreaves, Zohrab A. Samani, 1985. Reference Crop Evapotranspiration from Temperature. *Applied Engineering in Agriculture*  
476 1, 96–99. URL: <http://elibrary.asabe.org/abstract.asp?JID=3&AID=26773&CID=aeaj1985&v=1&i=2&T=1>, doi:10.13031/2013.26773.
- 477
- 478 Gilmer, J., Schoenholz, S.S., Riley, P.F., Vinyals, O., Dahl, G.E., 2017. Neural message passing for Quantum chemistry, in: Proceedings of the 34th  
479 International Conference on Machine Learning - Volume 70, JMLR.org, Sydney, NSW, Australia. pp. 1263–1272.
- 480 Kipf, T.N., Welling, M., 2017. Semi-Supervised Classification with Graph Convolutional Networks. URL: <https://openreview.net/forum?id=SJU4ayYg1>.
- 481
- 482 Li, S., Du, T., Gippel, C.J., 2022. A Modified Fu (1981) Equation with a Time-varying Parameter that Improves Estimates of Inter-annual Variability  
483 in Catchment Water Balance. *Water Resources Management* 36, 1645–1659. URL: <https://doi.org/10.1007/s11269-021-03057-1>,  
484 doi:10.1007/s11269-021-03057-1.
- 485 Li, Y., Yu, D., Liu, Z., Zhang, M., Gong, X., Zhao, L., 2023. Graph Neural Network for spatiotemporal data: methods and applications URL:  
486 <https://arxiv.org/abs/2306.00012>, doi:10.48550/ARXIV.2306.00012. publisher: arXiv Version Number: 1.
- 487 Liang, X.X., Gloaguen, E., Claprood, M., Paradis, D., Lauzon, D., 2025. Graph Neural Network Framework for Spatiotemporal Groundwater  
488 Level Forecasting. *Mathematical Geosciences* 57, 1071–1093. URL: <https://doi.org/10.1007/s11004-025-10194-5>, doi:10.1007/s11004-025-10194-5.
- 489
- 490 Lin, H., Gharehbaghi, A., Zhang, Q., Band, S.S., Pai, H.T., Chau, K.W., Mosavi, A., 2022. Time series-based groundwater level forecasting  
491 using gated recurrent unit deep neural networks. *Engineering Applications of Computational Fluid Mechanics* 16, 1655–1672. URL:  
492 <https://doi.org/10.1080/19942060.2022.2104928>, doi:10.1080/19942060.2022.2104928. publisher: Taylor & Francis \_eprint:  
493 <https://doi.org/10.1080/19942060.2022.2104928>.
- 494
- 495 Mohammad, S., Islam, A., Shit, P.K., Towfiqul Islam, A.R.M., Alam, E., 2023. Groundwater level dynamics in a subtropical fan delta region and its  
496 future prediction using machine learning tools: Sustainable groundwater restoration. *Journal of Hydrology: Regional Studies* 47, 101385. URL:  
497 <https://www.sciencedirect.com/science/article/pii/S2214581823000721>, doi:10.1016/j.ejrh.2023.101385.
- 498
- 499 Mukherjee, A., Coomar, P., Sarkar, S., Johannesson, K.H., Fryar, A.E., Schreiber, M.E., Ahmed, K.M., Alam, M.A., Bhattacharya, P., Bundschuh,  
500 J., Burgess, W., Chakraborty, M., Coyte, R., Farooqi, A., Guo, H., Ijumulana, J., Jeelani, G., Mondal, D., Nordstrom, D.K., Podgorski, J.,  
501 Polya, D.A., Scanlon, B.R., Shamsudduha, M., Tapia, J., Vengosh, A., 2024. Arsenic and other geogenic contaminants in global groundwater.  
Nature Reviews Earth & Environment 5, 312–328. URL: <https://www.nature.com/articles/s43017-024-00519-z>, doi:10.1038/s43017-024-00519-z. publisher: Nature Publishing Group.
- 502 Nayak, P.C., Satyaji Rao, Y., Sudheer, K., 2006. Groundwater Level Forecasting in A Shallow Aquifer Using Artificial Neural Network Approach.

- 503 Water Resources Management 20, 77–90. doi:[10.1007/s11269-006-4007-z](https://doi.org/10.1007/s11269-006-4007-z).
- 504 Refsgaard, J.C., 1997. Parameterisation, calibration and validation of distributed hydrological models. Journal of Hydrology 198, 69–97. URL:  
<https://www.sciencedirect.com/science/article/pii/S002216949603329X>, doi:[10.1016/S0022-1694\(96\)03329-X](https://doi.org/10.1016/S0022-1694(96)03329-X).
- 505 Rodell, M., Houser, P.R., Jambor, U., Gottschalck, J., Mitchell, K., Meng, C.J., Arsenault, K., Cosgrove, B., Radakovich, J., Bosilovich, M., Entin,  
506 J.K., Walker, J.P., Lohmann, D., Toll, D., 2004. The global land data assimilation system. Bulletin of the American Meteorological Society 85,  
507 381–394.
- 508 Sahili, Z.A., Awad, M., 2023. Spatio-Temporal Graph Neural Networks: A Survey. URL: <http://arxiv.org/abs/2301.10569>, doi:[10.48550/arXiv.2301.10569](https://doi.org/10.48550/arXiv.2301.10569). arXiv:2301.10569 [cs].
- 509 Sahoo, S., Jha, M.K., 2013. Groundwater-level prediction using multiple linear regression and artificial neural network techniques: a com-  
510 parative assessment. Hydrogeology Journal 21, 1865–1887. URL: <https://doi.org/10.1007/s10040-013-1029-5>, doi:[10.1007/s10040-013-1029-5](https://doi.org/10.1007/s10040-013-1029-5).
- 511 Scanlon, B.R., Fakhreddine, S., Rateb, A., de Graaf, I., Famiglietti, J., Gleeson, T., Grafton, R.Q., Jobbagy, E., Kebede, S., Kulu, S.R., Konikow,  
512 L.F., Long, D., Mekonnen, M., Schmied, H.M., Mukherjee, A., MacDonald, A., Reedy, R.C., Shamsuddoha, M., Simmons, C.T., Sun, A.,  
513 Taylor, R.G., Villholth, K.G., Vörösmarty, C.J., Zheng, C., 2023. Global water resources and the role of groundwater in a resilient water  
514 future. Nature Reviews Earth & Environment 4, 87–101. URL: <https://www.nature.com/articles/s43017-022-00378-6>, doi:[10.1038/s43017-022-00378-6](https://doi.org/10.1038/s43017-022-00378-6). publisher: Nature Publishing Group.
- 515 Scarselli, F., Gori, M., Ah Chung Tsoi, Hagenbuchner, M., Monfardini, G., 2009. The Graph Neural Network Model. IEEE Transactions on Neural  
516 Networks 20, 61–80. URL: <http://ieeexplore.ieee.org/document/4700287/>, doi:[10.1109/TNN.2008.2005605](https://doi.org/10.1109/TNN.2008.2005605).
- 517 Sophocleous, M., 2002. Interactions between groundwater and surface water: the state of the science. Hydrogeology Journal 10, 52–67. URL:  
<https://doi.org/10.1007/s10040-001-0170-8>, doi:[10.1007/s10040-001-0170-8](https://doi.org/10.1007/s10040-001-0170-8).
- 518 Sun, J., Hu, L., Li, D., Sun, K., Yang, Z., 2022. Data-driven models for accurate groundwater level prediction and their practical significance  
519 in groundwater management. Journal of Hydrology 608, 127630. URL: <https://www.sciencedirect.com/science/article/pii/S0022169422002050>, doi:[10.1016/j.jhydrol.2022.127630](https://doi.org/10.1016/j.jhydrol.2022.127630).
- 520 Taccari, M.L., Wang, H., Nuttall, J., Chen, X., Jimack, P.K., 2024. Spatial-temporal graph neural networks for groundwater data. Scientific Reports  
521 14, 24564. URL: <https://www.nature.com/articles/s41598-024-75385-2>, doi:[10.1038/s41598-024-75385-2](https://doi.org/10.1038/s41598-024-75385-2). publisher: Nature  
522 Publishing Group.
- 523 Talib, A., Desai, A.R., Huang, J., 2024. Spatial and temporal forecasting of groundwater anomalies in complex aquifer undergoing climate and land  
524 use change. Journal of Hydrology 639, 131525. URL: <https://www.sciencedirect.com/science/article/pii/S0022169424009211>,  
525 doi:[10.1016/j.jhydrol.2024.131525](https://doi.org/10.1016/j.jhydrol.2024.131525).
- 526 Taylor, R.G., Scanlon, B., Döll, P., Rodell, M., van Beek, R., Wada, Y., Longuevergne, L., Leblanc, M., Famiglietti, J.S., Edmunds, M., Konikow,  
527 L., Green, T.R., Chen, J., Taniguchi, M., Bierkens, M.F.P., MacDonald, A., Fan, Y., Maxwell, R.M., Yechieli, Y., Gurdak, J.J., Allen, D.M.,  
528 Shamsuddoha, M., Hiscock, K., Yeh, P.J.F., Holman, I., Treidel, H., 2013. Ground water and climate change. Nature Climate Change 3, 322–  
529 329. URL: <https://www.nature.com/articles/nclimate1744>, doi:[10.1038/nclimate1744](https://doi.org/10.1038/nclimate1744). publisher: Nature Publishing Group.
- 530 Wada, Y., van Beek, L.P.H., van Kempen, C.M., Reckman, J.W.T.M., Vasak, S., Bierkens, M.F.P., 2010. Global depletion of ground-  
531 water resources. Geophysical Research Letters 37. URL: <https://onlinelibrary.wiley.com/doi/abs/10.1029/2010GL044571>,  
532 doi:[10.1029/2010GL044571](https://doi.org/10.1029/2010GL044571). \_eprint: <https://agupubs.onlinelibrary.wiley.com/doi/pdf/10.1029/2010GL044571>.
- 533 Wan, Z., Hook, S., Hulley, G., 2021. Modis/terra land surface temperature/emissivity 8-day l3 global 1km sin grid v061. NASA Land Processes  
534 Distributed Active Archive Center. URL: <https://doi.org/10.5067/MODIS/MOD11A2.061>, doi:[10.5067/MODIS/MOD11A2.061](https://doi.org/10.5067/MODIS/MOD11A2.061).

Short title

- 541 Wang, L., Jiang, Z., Song, L., Yu, X., Yuan, S., Zhang, B., 2024. A groundwater level spatiotemporal prediction model based on graph convolutional  
542 networks with a long short-term memory. *Journal of Hydroinformatics* 26, 2962–2979. URL: <https://doi.org/10.2166/hydro.2024.226>,  
543 doi:10.2166/hydro.2024.226.
- 544 Wu, Y., Mei, G., Shao, K., Xu, N., Peng, J., 2025. Forecasting Groundwater Level by Characterizing Multiple Spatial Dependencies  
545 of Environmental Factors Using Graph-Based Deep Learning. *Journal of Geophysical Research: Machine Learning and Computation*  
546 2, e2024JH000520. URL: <https://onlinelibrary.wiley.com/doi/abs/10.1029/2024JH000520>, doi:10.1029/2024JH000520.  
547 \_eprint: <https://agupubs.onlinelibrary.wiley.com/doi/pdf/10.1029/2024JH000520>.
- 548 Yu, B., Yin, H., Zhu, Z., 2018. Spatio-Temporal Graph Convolutional Networks: A Deep Learning Framework for Traffic Forecasting, in: Proceed-  
549 ings of the Twenty-Seventh International Joint Conference on Artificial Intelligence, pp. 3634–3640. URL: [http://arxiv.org/abs/1709.  
550 04875](http://arxiv.org/abs/1709.04875), doi:10.24963/ijcai.2018/505. arXiv:1709.04875 [cs].